

# High-Speed 3d Modelling from Premium Rebuilding of Solid State Models

Aykut Zongur

Project Office Directorate, Ministry of Energy, Ankara, Turkey; z.aykut@rocketmail.com

## Abstract

**Objectives:** We execute a work in a 3D setting and make projections from solid builders for 3D representations of 3D scenery to transition from 2D displays to 3D models. **Methods:** Constructional work of area-laying is the 3D model-driven real-world object modelling that starts from the acquisition of data in range format and passing to the transfer of them for transition modelling. Ranging-depth is the key-factor in the factorization of the depth-maps to the iso-surface values. Factorizing to building factors of 3D formation concerns settings of 3D rebuilding. Mid-depth ranging is a key factor in the factorization of iso-value/surface depth mapping. **Findings:** The dimension exchange transit passes through three axe-transitive passage build-up ranged frames. Multiple dimensions are entered to make a variety of reforms across a 3D overlay created by hand during state change transition. Having factorized to its building-blocks in 3-D, the only left matter to-do in our reform is to regulate the whole worlds of the 3-Dimensional rebuilding. With the state changes that fitting out in time varying mode, we could be able to fully rig-out the complete surface ground. The state change fits the surroundings in the time varying mode with skinning. Directed mapping produces a detailed 3D model of a surface domain area. The 3D modeling of solid objects cannot be finalized until it is made more efficient. Our proposed design approach is adaptively refining also the higher-order multi-variate problems with specially-recreation ways under certain boundary constraints for exceeding the status of former that is passed by our series of proposed techniques in multiphase structured solid work tests. **Applications:** The speed of reincarnation is in turn altered. This processing lasts shorter period of time at last and it will improve outcomes by transferring triangular structuring tiles faster through refined procedures.

**Keywords:** Computational Efficiency, 3D Rebuilding, Solid Modelling

## 1. Introduction

In computer-assisted design, a variety of rigid body models of varying degrees of detail are identified based on the model pose estimator for free body detection and model shape optimization for parameterized shape analysis. Form work models are estimated from 3D graphical forms of 3D virtual makings for virtual realization and from 3D builds with the integration of

frame series for augmented realities. Furthermore, in future reality systems, virtual (non) rigid body floors are covered with our content-rich layout designed for our new exhibition model. Our latest model involves the latest model-reshaping technique for our studio displays, and the model is determined from our simulation results. In the interest of supporting realism, visualization is geared toward the generation of visually appealing effects.

\*Author for correspondence

The redesigned model of object shapes can be applied in conjunction with methods of computer-aided design. Similar to many virtual creations, modeling is done by switching between two dimension variations and by obtaining object bodies as inputs. Switching between the two dimensions is done to switch between instances. Shape/pose switching can be used to accurately model object bodies. However, the spline curvatures of objects, which are not effective for modeling, fail to use the latest constructive tools for estimating body shapes. Reform drives are the most critical applications involving shape molds and are adaptively fit when reforming the base shapes of free bodies. Models that are reshaped during these reform periods are essential for imitating statues and for the shape estimation of bodies' underestimation.

In object surface rigging, statistical learning tools are used to rig the whole shape of a character<sup>1</sup>, generating timely results with little additional computational cost. In addition to the latest subjects, a particular mannequin body surface is also involved. In turn, each perspective is manually shaped under newer aspects of initialization for more precise detection. Stages mitigate challenges, excluding a parallel detector to make estimations by playing a leading role in the interchange. Our simulation demarcates boundaries and fits shapes to entire surfaces of characteristic properties of an object. These object body surfaces are skinned with our rigger and are fully rigged. The skins are rigged with skin frames that are optimized in one optimal series.

Throughout the rebuilding phase, we have explored the cascading of developmental processes based on respective properties: 1) the outlook appears real from the outside. They might not exhibit leveled and original realism and may show no need for fine granularity from one height to another (e.g., coarse granularity in self-folding). 2) Non-redundancy is setup as a trade-off for computational efficiency, and low levels of dimensionality are to be replaced in all phases of the parametric models parameterized over the determined facade. 3) An expansion pack for a broad arrange of extensions is to be created. For instance, the representational modes of adaptations are made generic for easier adaptation of varied object body shapes. The parametric models are used for adaptive performance in real time tests of specialized simulations, and in initial stages of performance, this allows for auto-locating. The process remains controlled over the course of virtual model recreation.

We use newer resolutions for well-posed problems to estimate object shapes in 3D with minimal levels of deformation. We model our object on 2D contours for the estimation of 2D shapes under noisy conditions. We take the estimator of the 3D data-driven constructor model and the feature selection for diversified curve-shaped models to new heights. These models are fully automated for automatic processing and are verified in the restoration of imitative 3D simulations. Finally, a restorative data-driven model for 3D stationary designation is developed from the representational assembly in preparation for auto-adapting simulation design generators. Self-adaptive modeling is used to refresh the graphics creations in advance.

## 2. Past Work

### 2.1. Statue of Model Parameter Estimation

Several studies have examined 2D/3D object body contours together with regular form images<sup>2,3</sup>. The shapes of pose estimates form the locating lines of object parts in particular locations detected with time-invariant parts and are used to shape makers or characterized designs<sup>4</sup>. Pose estimates are used to infer relative joint rotations found for local positioning for the inference of object part locations<sup>5</sup>. Body shapes originally refer to independent shape structures (e.g., height, weight, and waist size). A minor component of the parameterized 3D model is the firm representative of shapes and poses<sup>6</sup>. We eventually manipulate the shapes of bodies by configuring height postures.

In this section, we estimate shapes within noisy 3D frames using one available view and one frame<sup>7</sup>. Images are captured under noisy conditions while the process is lined across frames. We also describe our simplified rebuilding model based on our initial calibration, which increases 2D body shape estimation accuracy levels to rebuild object body surfaces<sup>8</sup>.

### 2.2 Surface Reshaping

Skinning is central to object shape modeling<sup>9</sup>. From the natural dynamic structure of skinned character shapes, we serialize depth mapping with a series for the restructuring of model shapes similar to special modeling<sup>10</sup>. Meanwhile, high-quality modeling involves a trade-off between optimization and costly building times. We manipulate the intended fields from normal estimations

found from detailed data-driven computational model variants, but the difference has also long been attributed to the lower dimensional surface and to an adaptation to a different object physique<sup>11</sup>. Once the model is detected from 3D estimates, its shape and capacity from factors render the model available for fitting to the estimated shapessurface<sup>12</sup>. We restructure the 3D model to an appropriate model to be compliant with restructuring blocks<sup>13</sup>. The restructured model is thus fully available with 3D elliptical equation limitations.

### 2.3 Challenges from the Past to Present

Shape estimations are created from one or multipreviews<sup>14</sup>. Serial images for varying shapes in room conditions arise with composite building assortments, such as lighting/shading, occlusion, viewpoints, and deformation. Deriving a shape from multiple object shape estimations is difficult because it is necessary to eliminate obscurities<sup>5</sup>. We optimally set an object shape apart from the environment from which it is formed from connected components. Depth viewing is one of the other methods that set the object apart from the environment. A ranged depth is the projection of the 3Dworld onto spherical coordinates based on depth information in direct recovery from the viewset<sup>15</sup>. This problem becomes even more complex when mirrored objects are a bell or flat shaped according to the viewer<sup>16</sup>. Issues of occlusion may pose another challenge. Facade/self-occlusion bears side effects on the registration of 3D pointsets<sup>17,18</sup>. Unknown backgrounds have always posed challenges. When attempting to launch quickly, it is difficult to contour the foreground accurately in estimating shape poses<sup>18,19</sup>.

Model simulations present several challenges. While classical simulation techniques are used to simulate bodies, this study presents the following challenges. First, in regard to computation<sup>20</sup>, solutions are of a higher resolution even though they are not processed in line with propulsion methods without machinery. Reference scenes in absolute references are unique to certain distances<sup>21</sup>. Under high levels of complexity, data-driven models employ learning techniques to map finer meshes<sup>15</sup>. Numerous intersected meshes from training sets and other testing sets are crossed-checked through cross-validation. There is room to improve resolutions that are more valued in priori estimates and posteriori estimations are underway. These products cannot be taken as examples of objects that are built up virtually rather

than on a base mesh. Manual treatment is occasionally required including manual application of fundamentals of design: “geometrical calibrating burden is overcome by the hand of readjustment and the manual reformation for the parametric 3D shape models”<sup>8,22</sup>. Both are concurrently applied manually. Adaptive reshaping is always employed. Distinct shapes are distinct forms apart from simulations<sup>22,23</sup>. Annexation is used to select manually the best-changing sizes and shapes of each object and to replace points in initial gradating locations<sup>24</sup>. Serial manufacturing of interconnected mesh can be realized by crossing our assorted concepts.

High-speed building is executed first. Refinement as an extra factor of recreation can involve dimension-reduced installment or not, and it must be carried out via light computations of a shorter timeinterval<sup>25</sup>. This time axial of an expressive articulation surface structure is the automatic setting of our higher speed simulator. Previous models are less efficient and exhibit mid-range low gear coarsegranularity<sup>26</sup>.

## 3. Detection and Localization

Advanced 3D concepts are based on point cloud building and on the generation of ranged data in 3D.

We had developed several methods for the processing of several images at the same time. Although we can use point clouds to carry out several tasks, we only explore the following areas: registration and surface rebuilding.

More processing is necessary to enable superiority over point clouds. We have developed point clouds for each frame work, and the point clouds are independent of one another. While it would be wise to associate these points with each distinctive point cloud, as one frame covers the left walls while the other frame surrounds the right walls, the two point clouds are seamed and set apart from one point cloud for triple coverage. The correct transformation alignment of dual points occurs through registration. This is necessary for the transformation of two point clouds and for adjustment for realignment.

3D information is widely availed in our special design. The internal structure of a building could be made available for floor planning across obstacles. Adapted schemes for locational interior architectures are essential for matching. When locational information for a point is fixed, its arbitrary trajectory can be followed. Using projection, we can determine locations and trajectories

through the center of the projection, and we can structurally map an object of interest. Simultaneously estimating both is not as simple.

The structure of the ambient is planned for an entire virtual path while exceeding hurdles. When we know the location and trajectory of the surrounding areas, solid-state object maps are restructured.

When a solid body is mapped as point clouds, we extract the surfaces of an object. When examining point clouds on a larger scale, solid-state objects are apparent. However, up close, points are distinct and disconnected. When new buildings are to be represented, the overall point structures and colors must be interpolated by fitting on one parametric solid surface to point clouds through our new procedures.

An equalizer model of the  $ax + by + cz + d = 0$  equation parameterizes planar surfaces with quad parameters. The best-fit depth maps of a principal scene plane are the main cause of problems related to the quaternary range interval.

$$A^{(n+1)} = \frac{\alpha_a F + \sum_i \alpha_i A^{(n-i)}}{\alpha_c}, \tag{1}$$

$a_a$ ,  $a_p$ , and  $a_c$  are the weights, and  $F$  is the value of each frame.

The outlier redundancy (the other terms for noisy points) and background elimination with RANSAC were used to convert sections of the infinite fitting plane equation to 3D. The locations of candidate objects are underground boundary values, namely, one from an estimated equation and one from the other side of the computed convex hull, which is totaled for the approxima-

tion of projections of all other forms over inliers<sup>27</sup>. These values, can be approximated through projection. The convex hull is the delimiter of the area in which objects are relocated. After filtering points not falling within the area, the 3D prism is rebuilt over the convex hull area. Points falling within or outside of the prism are then checked using geometrical checks.

## 4. Proposed Design Approach

### 4.1 Transition Modelling

As newcomers range in intensity, newer data from peripherals are of 2D intensity just as it is in Figure 1. The relationship between the exact depth (meters of distance from the emitter) and gauge specific DMap (measurement units from the appliance) is not a one-to-one relation just as illustrated in the Figure 2. When a relation that is not one-on-one is identified, real range data are related to equinity and distances are set. In turn, geometric calibrations are applied without blocking the path up from that point.

Unequal units are converted into meters using the following formula:

$$value(z) = \sqrt{((value(x, y))^2 + sc - dfo)}. \tag{2}$$

Where  $sc$  is the scale coefficient and  $dfo$  is the original distance coefficient. Conversions are based on two decisive coefficient parameters referred to as  $sc$  and  $dfo$ . The first parameter is responsible for scaling and second denotes the distance from the origins of all parameters for

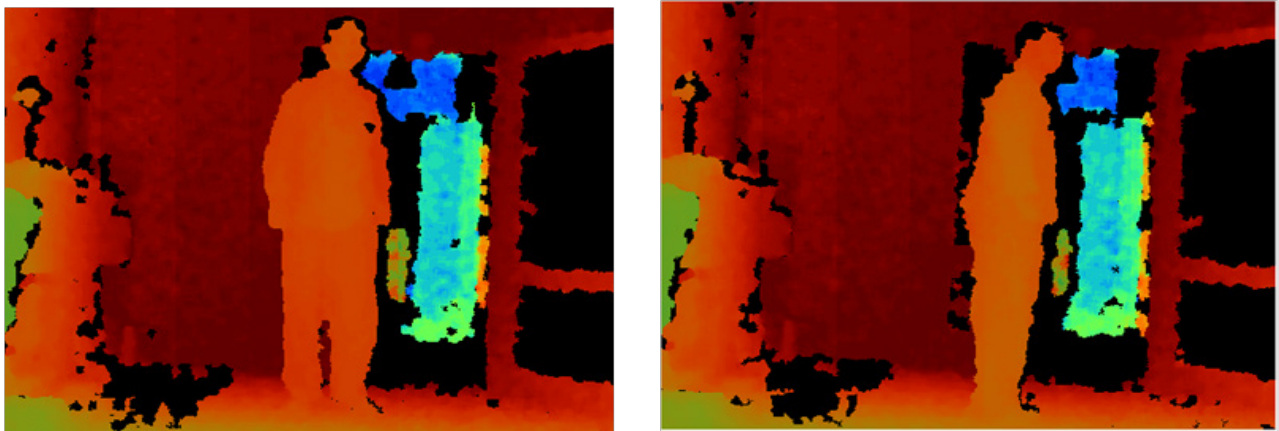


**Figure 1.** Depth maps from sensors and what we preprocess as in-depth tri-colored products

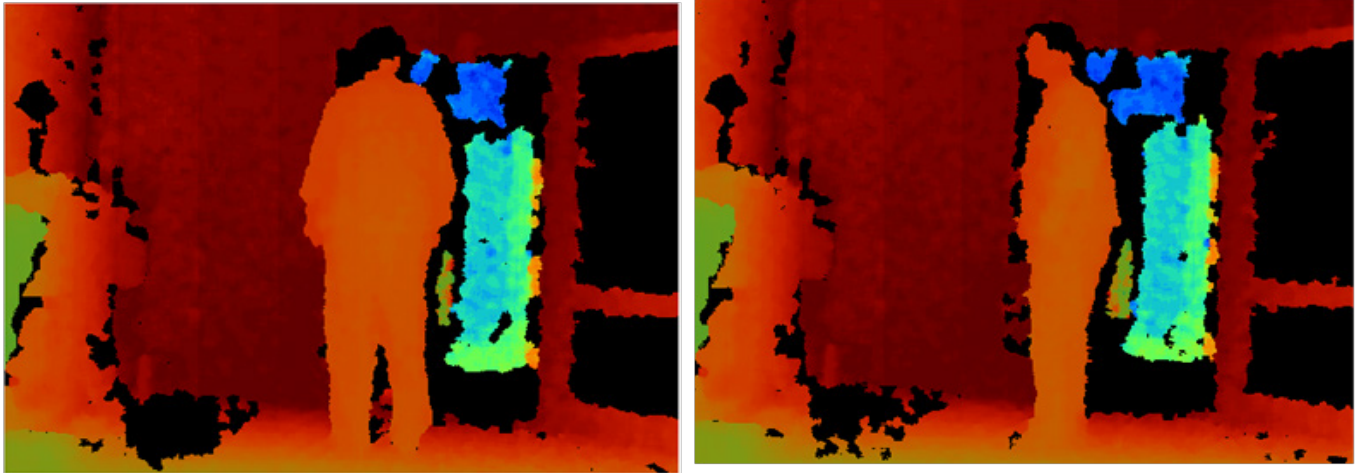


**Figure 2.** X: .. pixel + Y: .. pixel + Depth: .. mm := (2-D) RGB + (1-D) D = (3-D) RGB-D.

conversion. The conversion is determined by coefficients  $sc$  and  $dfo$ , which control the scale and origins of the conversion, respectively. The rig calibration is then followed by data post-processing. Procedural processing is carried out to increase accuracy levels. As conversion involves precise calibration, we apply a calibration procedure.

Once a decision on the coordinate is made, we can apply the pinhole geometric model for the second phase of tuning for coordinates  $x$  and  $y$ . We create point clouds from indicator measurements of depth readings. Our transformations are based on ranged images and point clouds. However, the methods to convert one to another are not always clear. Calibration data attained are thus useful from this point on.

- An initial-state of framing from one facade.
- From the perspective-view after one  $270^\circ$  rotational outlook.

$$\sum_{j=0}^{j=no\ of\ row} \sum_{i=0}^{i=no\ of\ col} Cloud \rightarrow z = (2), \tag{3}$$

$$Cloud_{x,y,z} \rightarrow x = z * \frac{i - p_x}{f_x}; \tag{4}$$

$$Cloud_{x,y,z} \rightarrow y = z * \frac{j - p_y}{f_y}; \tag{5}$$

$$Cloud_{x,y,z} \rightarrow z = value(z); \tag{6}$$

where  $f_x$  = focal length of X and  $f_y$  = focal length of Y. After all of these sequential-processing, our point cloud is formed in the following manner:

$$PC_p = D_p(\vec{\alpha}f) \cdot C_p(\vec{\beta}) \quad (p [1..P]) \tag{7}$$

Here this regular expression is assembled from the graphs of representatives in the Figures 3 and 4.

### 4.2 Registration Preparation

Datasets are formed from images, and when the model of representation is a 3D model or exists in either point cloud, registration occurs within the 3D coordinate system. Registration complexity levels change with task difficulty levels. Transformations can be of two classes. The first class of transformation involves simple translation while the other class can result in non-rigid and complex translation. Registration is best applied for panoramic view synthesis. Various scene images are collected for the creation of a panoramic image. In turn, registration estimates the relative image location and the alignment of overlapping areas.

Registration involves identifying a correct transformation for the alignment of two datasets. Transformation is applied to image coordinates. Homogeneous coordinates represent transformations of multiple matrices.

$$p' = T.p \tag{8}$$

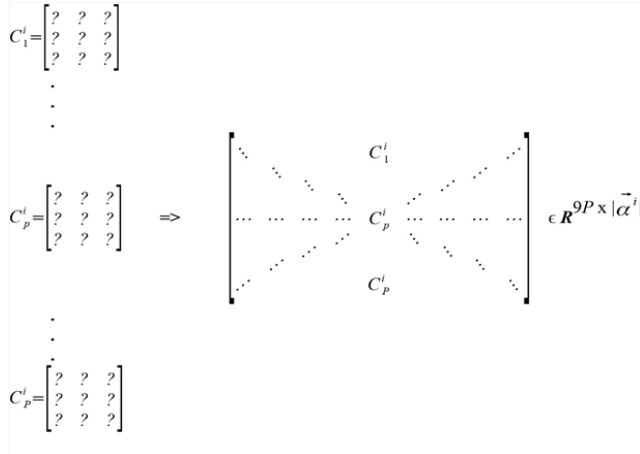


Figure 3. Point-clouds Adjacency Graph Formation.

Here, the  $p'$  vector represents the transformed coordinates. The  $T$  Matrix represents the transformation, and  $p$  represents the original coordinates. The structure of the transformation matrix changes with the transformation applied.

### 4.3 3D Registration

3D analysis was first carried out through 2D registration. Registration was initiated with the analysis of colorful and colorless images. The transformation estimation method is designed for images. Point relations are cut into and objects are tracked. Features are identified and descriptors are matched. We illustrate our feature-matching method based on two images of the same scene.

While automatic feature matching could also be deployed, the features of this matchup can be mismatched. This feature is mismatched as an outlier and accounts for a small number of cases. Keynote property also produces a very high number of errors. The outlier term creates numerous errors. This especially arises when estimating transformations. Dealing with these outliers is necessary because they are incorrectly matched as outliers. They represent a minor percentage of all matches and produce a significant number of errors in transformations, which are all assumed correct.

There are multiple variations and combinations of registration methods that vary in number. The representation represented by a transformation is applied to direct coordinates.

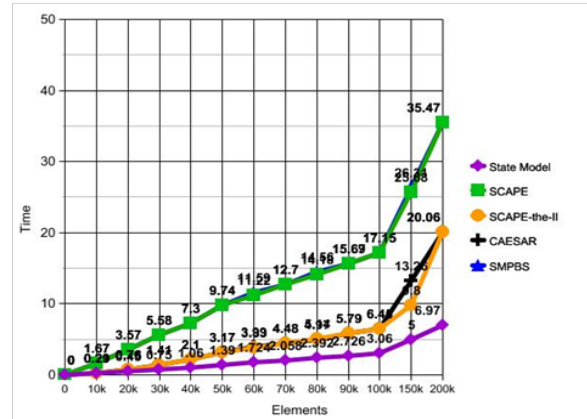


Figure 5. Timings of our Equation System Installation and Initialization Times for Reordering and Refactoring into Factors for Time Passed per.

$$\begin{bmatrix} x' \\ y' \\ z' \\ \mathbf{1} \end{bmatrix} = \begin{bmatrix} 1 & 0 & 0 & t_x \\ 0 & 1 & 0 & t_y \\ 0 & 0 & 1 & t_z \\ 0 & 0 & 0 & 1 \end{bmatrix} \cdot \begin{bmatrix} x \\ y \\ z \\ \mathbf{1} \end{bmatrix} = \begin{bmatrix} x + t_x \\ y + t_y \\ z + t_z \\ 1 \end{bmatrix}, \quad (9)$$

The estimation of ( $t_x$  and  $t_y$  and  $t_z$ ) transformation parameters is only possible for corresponding point couples. Only simpler alternative translations can be used to address inadequate matched points. Many more pairs can be used for general improvement purposes. In our study, the least mean square approach is applied for final estimation.

$$\begin{bmatrix} x_c \\ y_c \\ z_c \\ \mathbf{1} \end{bmatrix} = \begin{bmatrix} r_{1x} & r_{1y} & r_{1z} & 0 \\ r_{2x} & r_{2y} & r_{2z} & 0 \\ r_{3x} & r_{3y} & r_{3z} & 0 \\ 0 & 0 & 0 & 1 \end{bmatrix} \cdot \begin{bmatrix} x_d \\ y_d \\ z_d \\ \mathbf{1} \end{bmatrix} + \begin{bmatrix} t_x \\ t_y \\ t_z \\ \mathbf{1} \end{bmatrix}, \quad (10)$$

Transformative alternators can be derived from mean differential points yielding the best results.

$$t_x = \sum_{i=1}^N \frac{(x'_i - x_i)}{N}, \quad (11)$$

$$t_y = \sum_{j=1}^N \frac{(y'_j - y_j)}{N} \quad (12)$$

$$t_z = \sum_{k=1}^N \frac{(z'_k - z_k)}{N} \quad (13)$$

As an alternative to baseline transformations, we project the second image over the coordinate system of the first image. The results are based on view set samples. The images are frame worked as white/black images. Full-color overlays are used for reference images.

Translation is mainly required for image registration, although it is generally insufficient for registering. All images are rotated, scaled, and sheared. All general transformations are built on one affine transformation. The affine transformation is a  $4 \times 4$  matrix representation of  $[0, 0, 0, 1]$  in its last end row.

$$T_{transformation} \oplus T_{translation} = \sum_{i=1}^4 \sum_{j=1}^4 \begin{bmatrix} a_{ij} & a_{ij} & a_{ij} & t_x \\ a_{ij} & a_{ij} & a_{ij} & t_y \\ a_{ij} & a_{ij} & a_{ij} & t_z \\ \mathbf{0} & \mathbf{0} & \mathbf{0} & 1 \end{bmatrix}, \quad (14)$$

The matrix of affine transformation is represented by only 16 parameters. The dual matchup of a tri-point grading can be sufficiently exact to make estimations. This is true given that we can use more points to leverage negligible errors. We can fully revive the rotation and scaling operations for representational purposes. Affine overlay transformer functions are well matched to an original image.

3D transforms produce one homographic graph of a  $4 \times 4$  random matrix set on 17 degrees of freedom (where the scale irrelevancy is in homogeneous coordinates). The homograph of the flat plenary generates high-definition scene images from the original plane interrelations.

Registration was not possible unless image areas were sheared from edges. Thus, when a scene has a 3D structure, we cannot register it in 2D without deforming the image outlines. However, from inbound 3D data-like point clouds, we could identify the 3D transformation that can truly align points.

We apply rigid 3D transformation for self-rotation and translation. "Rigidity" denotes the degree to which an object does not change a model's shape with time. The other move reflects the rotation of the coordinate system. Rigid transformations occur in two points of nonhomogeneous coordinates.

$$\vec{c}' = R \cdot \vec{c} + T, \quad (15)$$

The  $R$  symbol is a  $4 \times 4$  orthonormal matrix that symbolizes rotation, and  $t$  is the  $4 \times 1$  vector of translation. For the estimation of transformation parameters, 3D point matches are required. When point clouds  $P$  and  $P'$  must

be addressed where each point  $\vec{c}$  has a counterpart point of  $\vec{c}'$ , we compute the rigid transformation between two points. These steps are computed through rotation and translation.

For rotation computation, we first subtract the mean location from each point cloud.

$$E(p) = \frac{1}{N} \sum_{p=1}^N \vec{c}_p, \quad (16)$$

$$\mu = e = \frac{1}{N} \sum_{p=1}^N \vec{c}_p, \quad (17)$$

$$\vec{c}_p = \vec{c}'_p - \mu, \quad (18)$$

that the problem is independent of translation, the resulting point clouds are rotationally related. Thus, the solution simplifies the problem. All cloud points are stacked onto the  $P$  matrix with a size of  $4 \times N$ , the columns represent one point, and the points are multiplied.

$$A = P(P')^T, \quad (19)$$

We extract a rotational parameterization from a matrix through the decomposition of SV unit elements. The extraction of rotational units from the matrix by SV decomposition is segmented into unit elements of matrix-forms<sup>28</sup>. The  $U$ ,  $S$ , and  $V$  matrices are sub-matrices.

$$USV^T = A, \quad (20)$$

The rotational formula is applied through feed forward formula for the expansion pack:

$$R = VU^T \quad (21)$$

After determining the rotation of the derivation, the translational formula is derived from the following equation:

$$T = e' - Re, \quad (22)$$

The equations shown are not as complex. From the consortium of languages, equations are written based on different taxonomy names.

The design and implementation are based on the orientations of 3D points. The two point clouds set at the orientation of the three points are extracted.

Our initial classes exhibit an advanced registration functioning for point clouds. We design an iterative closest point algorithm for superior performance. Older methods

take much longer to generate iterations. Expected values are generated faster when using our high-performance method. Results derived from our newly developed techniques are far superior. Our design can be used to solve more heavyweight problems that could not be solved easily previously. Our approach works well and is efficient when applied to these problems.

Many points occasionally go off track; therefore, the least squares fitting method may or may be not the best approach. Fitting involves the use of an initially parametric model for datasets with fewer outliers, and classical outlier detection routines are regularly used in circuits. Up to three points of a 3D plane are adequate for the estimation of planar equations. Classical RANSAC tools draw on three random points in each iterative scheme.

$$SD [((\log(1 - w^n))^k) / \log(1 - w^n)], \quad (23)$$

$$\frac{\sqrt{(1 - w^n)}}{w^n}, \quad (24)$$

Here,  $SD(k)$  is the standard deviation of “ $k$ ”,  $n$  is the minimum number of points,  $k$  is the number of required steps, and  $w$  is the rational ratio of points.

Depth estimations are made more efficiently by applying partial differential views from different perspectives. The levels of efficiency can be improved by fixing reference points through estimations of different depths.

The expected value of unvarying sequential frames can result in radical increases in speed. The expectance of coherence is unclosed to consecutive frames drifted to the degree of efficiency increase. This process could be yielded through “Super Quick Ranging,” and the “Fast Fusion Transformation” could be relocated to the center of the project. This fusion works in “Superfast” ways and atomicity fusion directly projects through the center.

Algorithm 1: High-performance design with dimension-reduction of the redundant elements

*The new solution method minimizes the fills-in by guaranteeing fewer non-zero elements*

Input: Adjacency Graphs of structuring elements

1.  $G :=$  Formed Graph;
2. **while**  $G \neq \emptyset$  **do**
3.     Select the Minimum Degree  $i$  Node in  $G$ ;
4.     Order the  $i$  in order;
5.      $G := G_i$ ;
6. **end while**;

Output: Maximum possible nonzero-element triangular composite graph

The plane with the most inliers is used, and the plane equation is refined through least squares fitting with inliers.

## 5. Technical Framework Proposed

### 5.1 Estimations of Area Orientations

Although every point cloud is commissioned, we estimate the normal directions of surfaces from cloud point locations. We have created special class routines that function as sub-routines. The written classes identify the nearest neighbors of each point and fit planes. Normal local surfaces are defined as plane normal in this context. Our technical functions momentarily use the closest neighbors by neglecting distances. From this point, we can estimate the directions of normal through our functioning technique. Our functional methods work well for point clouds with density levels that are high in ambience, but rougher estimations are made for surrounding sparse point clouds. We have designed more specific means of estimating normal from point clouds. Normal estimations are made from our written routines as stated previously. The nearest neighbor for each point is determined and fitting planes are identified.

#### Algorithm 2: Algorithm for the estimation of normals

*The normal estimation of point cloud surfaces*

**Input:** PointXYZ // Initial known candidate points

**OcTree** < **new(OcTree)**; // A newer search tree has been recreated

**OcTree** < **Cloud**; // Allocate the cloud over the octal tree **while** searching to the closest octree **do** // the point count is set to 20

**Knn(octree)**; // invoke the kclosestneighborhood algorithm

**Normal\_Estimate(\*normals)**; // normals are to be calculated

**end while**

**Output:** cloud normals // surface normal

We have developed a special plan for triangular meshes with normal line estimates from point clouds. The major challenge here is related to determining which vertices are connected and which are unconnected. Inter-distances

of the identified vertices are not the only criteria used to determine the scalability or density of point clouds that are variants of our rebuilding directives. Nearest neighbor reconnections are much more important to follow and special attention must be paid to intersections between these surfaces. The timelines for the model factoring are plotted in Figure 5.

### 5.2 Surface Rebuilding

For the point clouds of certain objects, surface extraction involves some basic requirements. Surfaces are efficient relational object geometry representations. A surface refers to the geometry of represented objects. It is well that lower curved areas are to be represented with fewer vertices, but in contrast, many more vertices are included in detailed area representations. In addition, surfaces continuously define worlds, enabling self-interpolation between vertices; therefore, there is still too much to do for even one point cloud. One reference-model that we want to excel is the standard SCAPE<sup>29</sup> model and the runner-up model that comes in second place is the CAESAR<sup>30</sup>-model and the trailer is the body shape recreation of statistical model<sup>31</sup>. Our comparative chart (Table 1) with the quantitative approach is right out there.

All surfaces are trailed by one set of vertices and by a cluster of links. Each vertex has a 3D location close to the RGB trio and/or general tactile coordinates for color and for normal information. The direction normals are not normally gauged with a depth ranger by single normals and are generally estimated locally. Thus, the indicator link set for vertices is linked to the expression of surfaces. The topology of surfaces meets the topological conditions organized in triangles with a finite number of connected elements sharing two common vertices of interlacing surface expression.

$$\nabla v = \langle \partial v, \partial v, \dots, \partial v \rangle \tag{25}$$

$$\partial \xi_1 \partial \xi_2 \quad \partial \xi_v$$

$$\nabla \cdot \nabla v + \phi = 0 \quad \text{iv } \Omega \tag{26}$$

$$\nabla^2 v = -\phi \tag{27}$$

Majority of our techniques deployed here are all used in advanced stages. Our written classes for point clouds drive classes that are especially written for processed point clouds. We also illustrate our two techniques based

on a template. Here, triangulation and quad angulation are based on polygonization techniques.

$$\frac{u_{x-1,y,z} - 2u_{x,y,z} + u_{x+1,y,z}}{\Delta x^2} + \frac{u_{x,y-1,z} - 2u_{x,y,z} + u_{x,y+1,z}}{\Delta y^2} + \frac{u_{x,y,z-1} - 2u_{x,y,z} + u_{x,y,z+1}}{\Delta z^2} = f_{x,y,z} \tag{28}$$

Subject to:

$$(2, 2, 2) \leq (x, y, z) \leq (X, Y, Z) \tag{29}$$

So as to:

Total # of Unknowns =

$$\sum_{i=1}^N \frac{[(N-i+1)](N-i+2)}{2} = \frac{N(N+1)}{4} + \frac{1}{2} \sum_{i=1}^N i^2 \tag{30}$$

$$\Delta u \equiv \nabla^2 u = \nabla \cdot \vec{V} \text{ over } \vec{V}: \text{Vector Field} \tag{31}$$

$$V = \{ 0 < x < X, 0 < y < Y, 0 < z < Z \} \tag{32}$$

$$u = \begin{pmatrix} v \\ p \\ q \end{pmatrix} \tag{33}$$

$$u(x, y, z) = v(x) \cdot p(y) \cdot q(z) \tag{34}$$

## 6. Experimental Results

The simulation results were generated from an Intel Pentium (4) 3.0 Clock Cycle GHz CPU 12 GB RAM computer station. Our test scenarios were simulated on an NVIDIA GeForce 4 GB and high-end graphics video card. The more powerful the computer-processing unit we have, the more swift simulations can be done according to solo-wise frame working that enables rapid testing of the modeling. Our rebuilt finite state models are figured out in the illustration of Figure 6.

**Table 1.** Our readjustments for the space discretization of the polygonization computation Table

	Minimum Mesh-Space after the pre-processing	Reordering of the Building Blocks (s)	General-Factorization to discretized-points (s)
Our State of the Model	31502	1,46	4,85



**Figure 6.** Recreated Solid Models Manufactured via the Range Map Technique.

SCAPE Model	12500	0,14	2,01
Model of SCAPE-the-II	11256	0,5	3,65
CAESAR Model	7157	0,31	2
SMPBS	6890	0,08	1,09

- Our solid shape model.
- Rebuilt surface from the plan.

We present a resolution proposal for our initial time-dependent problem for faster estimation of a newer object model reshaped from perspective views. Our approximation preconditions customized 3D shape estimates of parameterized representative models, which are quickly rebuilt through multi-sided optimal relaxation via the one panoramic view and rapid simulation. Dimensional structural modeling involves rebuilding object model shapes from finite elements through initialization. Parametric modeling is reformulated to recover restructured shapes from the synthesized model based on ranged mapping. We reinforce a varied dimensional space by means of a multi-linear model once the dimensionally reduced time guard customization is activated for 3D models. We base our equations on symmetric and positive definite matrix systems<sup>27</sup>. The plotting for the computational times is charted as the times diagram of the time-series in the Figure 7.

In the body-surface skinning, the self-learning technics are utilized in rigging the whole body of the character,

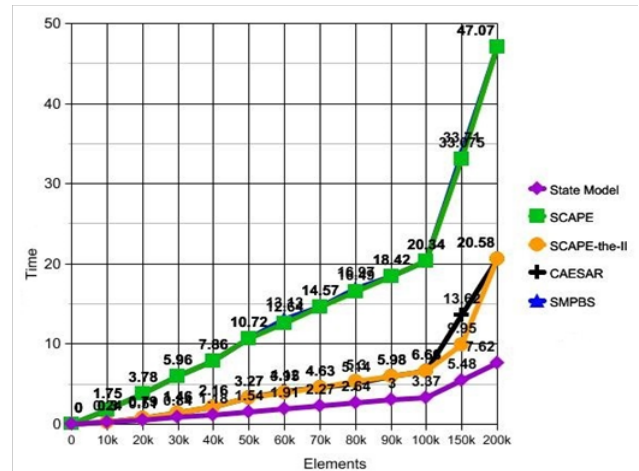


**Figure 7.** Computation Times of our Performance Boosting Technique Running with the Inclusion of our Highly Performed Solution.

providing lots of advantages for most possible optimized-result with lesser-additional computational costs. In the processing of them either, an one particular subject body-surfaces get involved in the final-product of the mannequins. And the newer aspects get shape under each perspective views of us for a maximum precise-detection by our manual-mode of refinement. The stages draws back the challenges with the exclusion of the local maxima-detections in estimating the global maximums in lieu of them. And this plays an inter-changeably leading role in parallel to object detection. The test of the rebuilding is firstly demarcating the boundaries and secondly fitting the new flooring onto the worked field for making it have an outfit over the whole surfaces of the subjects. And the subject surfaces are fully-rigged with our skinning procedures for the characteristic-properties in overall. The skins are getting rigged with the skin-toppings that are optimized-in one optimal-series of skinning. Our latestis leaving from the others ason view in the Table 2.

The involution of the object shape-modelling is an essence for the skinning process. By naturally from the natural-dynamic structure of the shape surface skinning, we serialize our special modelling over series of arrangements with the restructuring modellers for the object shapes in depth-mapping. On the other view, modelling is simulated in a high-end reconfiguration with the trade-off between highly-optimized configuration versus costly building-times. We manipulate the intended-fields with

**Table 2.** Our Model Features compared to other Physical Assessment Methods

	Average Number of Elements (the mesh-size)	Total Computation Times for the System (in seconds unit)	Average Speed Timing of the General Total (finite no. of element/s)
Our State of the Model	182912	6,9	26508,99
SCAPE Model	12500	2,26	5530,97
Model of SCAPE-the-II	65359	4,3	15199,77
CAESAR Model	41554	2,4	17314,17
SMPBS	6890	1,23	5601,63

the normal-estimation that found and we offered our new computational-model up to the finest-details and further more. But the main streamline of the two variants is exactly related with the installed automatic-conditioner that is liable of laying over the lower-dimensional surface of the interested object physique. Once the model is detected from the 3-D estimates, it is its shape that makes it available for fitting the estimated iso-value to the iso-surfaces. What enables the model for fitting is its ability that comes from the shape-factors. We're molding the 3-D model in an appropriate mode of compliance with the building blocks. And the restructured model is in full-availability with the 3-D elliptic-equational conditions. We built out solidstructuredmanufacturesfor the state of our modelsjustlikein the illustrative figuresin the Figure 8 underneath.

- Posting with clothes on.
- One Panoramic View.

## 7. Conclusion

In this study, a full workflow from 3D shape depths, to model building through accelerated rebuilding supplemented with quick retouching is given. This proprietary technique-supplemented approach generates detailed and customized outcomes. We thus illustrate the computerized modeling of real3D objects.

We presented our set of time values based on elliptical equation systems that are reclined to our functional models through two-directional contour lines. These function

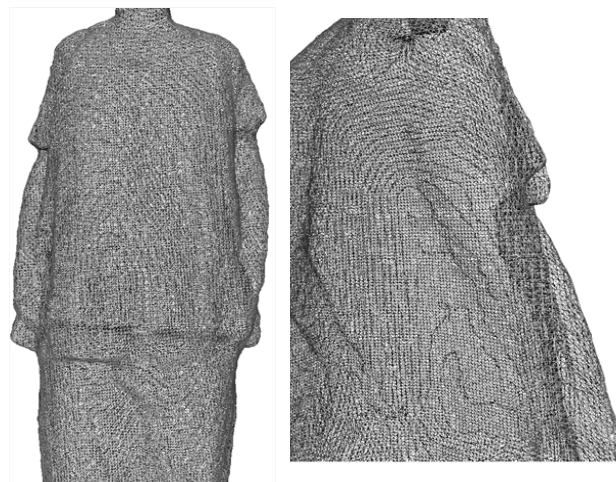


**Figure 8.** Making Operations on Surface Areas.

models are superior to initial delimitations of boundary values in the post-inference of solid shape skinning in the3D definition. 3Dmodels involve reshaped modeling with grid remising over solid models, are highly efficient, and statistically analyze eliminated outlier spatial axes effectively. The method augments upfront inference estimates from intercepted rebounding time constraints. The equation involves a3D system of elliptical equations with mixed boundary limits, and the boundary constraints were rebounded to timelines initialized to the initial set on time.

The 3D elliptical equation system is automatically built based on a 3D grid, and real viscous objects are synthesized in any shape. This generates a factorized model of object shapes with are built dependent synthesizer model based on the factorization of the object model. The intercepted model is resolved using direct and iterative solvers conditioned for efficiency. The need for preconditioning extends beyond the need for multi-dimensional solutions. We approximated a roughly time direct solution more accurately than the preconditioned Cholesky factorized equation. This approximation is required for minimum equation system requirements, whereby the representation of the model shapes takes matrix forms solved in 3D grids forming 3Dshape estimates of 3Dmodels taken based on the number of real factors. The result is simulated in seconds rather than minutes through more efficient processing. Our new models save time in processing time-dependent hybrid elliptic equations once they are regulated, and the rebuilding process is efficient while maintaining the levels of quality. In turn, we address problems of time indepen-

dent optimization. We balance realism with dynamism through our model, eliminating effects of least squares fitting. Our 3D model based on triple and double accelerated system agglomeration can be applied to a complete grid system and for the solidification of shape models.

## 8. References

1. Capell S, Duchamp T, Popovic Z. Physically based rigging for deformable characters. *Graph. Models*. 2007; 69(1):71-87. Crossref
2. Sun M, Kohli P, Shotton J. Conditional regression forests for human pose estimation. *CVPR*. 2012; p. 1-8.
3. Pons-Moll G, Taylor J, Shotton J, Hertzmann A, Fitzgibbon A. Metric regression forests for human pose estimation. *BMVC*. 2013; p. 1-11. Crossref
4. Carter J, Heath B. *Somatotyping – development and applications*. Cambridge University Press: England, 1990.
5. Barron C, Kakadiaris IA. Estimating anthropometry and pose from a single image. *IEEE Computer Society*. 2001; 81(3):269-84.
6. Szeliski R, Lavallée S. Matching 3-D anatomical surfaces with non-rigid deformations using octree-splines. *IEEE Workshop on Biomedical Image Analysis*. 1994; p. 144-13. Crossref
7. Hilton A, Starck J. From 3D shape capture to animated models. *International Symposium of 3D Data Processing, Visualization, and Transmission*. 2002; p. 1-10.
8. Deville JC, Sarndal C. Calibration Estimators in Survey Sampling. *Journal of the American Statistical Association*. 1992; 87:376-82. Crossref
9. Lewis JP, Cordner M. Pose space deformations: A unified approach to shape interpolation and skeleton-driven deformation. *ACM Press. Longman*. 2000; p. 165-72. Crossref
10. Yamasaki T, Aizawa K. Fast and Robust Motion Tracking for Time-Varying Mesh Featuring Reeb-Graph-Based Skeleton Fitting and Its Application to Motion Retrieval. *IEEE International Conference on Multimedia*. 2007; p. 2010-13.
11. Churchill E. *NASA Reference Publication 1024, The Anthropometry Source Book*. 1978; p. 1.
12. Lee AWF, Sweldens W. MAPS: Multi resolution adaptive parameterization of surfaces. *ACM Press Computer Graphics Proceedings*. 1998; p. 95-104. Crossref
13. Bronstein A, Kimmel R. *Springer: Numerical geometry of non-rigid shapes*. 2009; p. 11-40. Crossref PMID:19386136 PMCID:PMC2686732
14. Ma Y, Soatto S, Kosecka J, Sastry S. *Springer Verlag: An Invitation to 3D Vision*. 2003.
15. Kim VG, Lipman Y. Blended intrinsic maps. *ACM Trans. Graph*. 2011; 30(4):79. Crossref
16. Feldmar J, Ayache N. Rigid and affine registration of smooth surfaces using differential properties. *ECCV*. 1994; 801:396-406. Crossref
17. Besl P, McKay N. A method for registration of 3-D shapes. *PAMI*. 1992; 14(2):239-56. Crossref
18. Myronenko A, Song XB. Point-set registration: Coherent point drift. *TPAMI*. 2010; 32(12):2262-75. Crossref PMID:20975122
19. Liu Y. Automatic registration of overlapping 3d point clouds using closest points. *Image and Vision Computing*. 2006, 24(7):762-81. Crossref
20. Schenk O, Gartner K. On fast factorization pivoting methods for symmetric indefinite systems. *ETNA*. 2006; p. 58-179.
21. Gilbert E, Johnson DW. A fast procedure for computing the distance between complex objects in three-dimensional space. *IEEE Journal of Robotics and Automation*. 1988; 4(2):193-203. Crossref
22. Li H, Guibas L. Robust singleview geometry and motion reconstruction. *ACM Trans. Graph*. 2009; 28(5):175. Crossref
23. Shotton J, Fitzgibbon A, Cook M, Sharp T, Finocchio M, Moore R, Kipman A, Blake A. Real-time human pose recognition in parts from single depth images. *CVPR*. 2011; p. 1297-1304. Crossref
24. Zhang Z. Iterative point matching for registration of free form curves and surfaces. *International Journal of Computer Vision*. 1994; 13(2):119-52. Crossref
25. Ferrari V, Zisserman A. Progressive search space reduction for human pose estimation. *CVPR*. 2008; pp. 1-8. Crossref
26. Robinette KM, Boehmer M, Fleming S, Burnsides D. *US Air Force Research Laboratory: USA: Civilian American and European Surface Anthropometry Resource Technical Final Report*. 2002, p. 1-70.
27. Barber C, Huhdanpaa T. The Quickhull Algorithm for Convex Hulls. *ACM Transactions on Mathematical Software*. 1996; 22(4):469-83. Crossref
28. Lathauwer LD, Moor BD, Vandewalle J. A Multilinear singular value decomposition. *SIAM Journal of Matrix Analysis Applications*. 2000; 21:1253-78. Crossref
29. Anguelov D, Srinivasan P, Koller D, Thrun S, Rodgers J, Davis J. Scape: shape completion and animation of people. *ACM Trans. Graph*. 2005 July; 24(3): 408-16. Crossref
30. Robinette KM, Paquet E. The CAESAR project: A 3-D surface anthropometry survey. *Conf. 3D Digital Imaging and Modeling*. 1999; p. 380-86.
31. Hasler N, Stoll C, Sunkel M, Rosenhahn B, Seidel HP. A statistical model of human pose and body shape. *Computer Graphics Forum*. 2009; p. 1-10. Crossref